Nano Energy 69 (2020) 104455

Contents lists available at ScienceDirect

Nano Energy

journal homepage: http://www.elsevier.com/locate/nanoen

Full paper

NbO_x nano-nail with a Pt head embedded in carbon as a highly active and durable oxygen reduction catalyst

Zhong Ma [a], Shuang Li [b], Lijun Wu [c], Liang Song [d], Gaopeng Jiang [a], Zhixiu Liang [d], Dong Su [b], Yimei Zhu [c], Radoslav R. Adzic [d], Jia X. Wang [d,**], Zhongwei Chen [a,*]

[a] Department of Chemical Engineering, Waterloo Institute for Nanotechnology, University of Waterloo, Waterloo, Ontario, N2L 3G1, Canada
[b] Center for Functional Nanomaterials, Brookhaven National Laboratory, Upton, NY, 11973, USA
[c] Condensed Matter Physics and Materials Science Division, Brookhaven National Laboratory, Upton, NY, 11973, USA
[d] Chemistry Division, Brookhaven National Laboratory, Upton, NY, 11973, USA

ARTICLE INFO

Keywords:
Pt
NbO_x
Strong metal-support interaction
Surface pore
Selectively deposition

ABSTRACT

Further enhancing activity and durability of Pt-based catalysts for oxygen reduction is needed for the automotive application of fuel cells. This is however a very challenging task. Herein, we describe a new method to nail down low-oxidation-state NbO_x nanoparticles at high temperature without overgrowth using the surface pores on carbon and then deposit Pt head selectively on top of NbO_x derived by the redox reduction between themselves. This new structured catalyst, Pt-NbO_xC, exhibited mass activities higher than 0.5 A mg^{-1} after 50,000 cycles between 0.6 and 1.0 V and 5,000 cycles between 1 and 1.5 V, which are 7 and 4 times of the 0.07 and 0.13 A mg^{-1}, respectively, on Pt/C. That high sustainable ORR activity is ascribed to strong metal-support interaction that maximizes Pt utilization and minimizes particle agglomeration, carbon corrosion and metal oxidation. Furthermore, the method embedded nanoparticles into carbon pores will likely be used in developing small particles with uniform dispersion for various applications.

1. Introduction

Building sustainable clean energy system is one of the most critical challenges facing humanity today [1–3]. Polymer electrolyte membrane fuel cell (PEMFC) is a clean energy technology which, with its automotive applications, can make a major contribution to such a system [4–8]. PEMFCs use platinum-based catalysts as the most suitable choice to overcome the problems caused by the sluggish kinetics of oxygen reduction reaction (ORR), and inadequate stability of oxygen cathodes, which reduce performance efficiency of PEMFC and hamper their broad applications [9,10]. Intensive theoretical studies have been devoted to increase the understanding of ORR mechanism and to enhance the reaction kinetics. These helped at maximizing utilization of Pt atoms and tuning their electronic structure [11,12] that resulted in recent development of practical catalysts, such as supported catalysts [13,14], Pt-transition metals alloys [15–18], Pt monolayer electrocatalysts [19,20], core-shell [21–25] and shape controlled catalysts [26–28].

While great improvements of activities of Pt-based catalysts have been achieved, catalyst durability remains an issue, especially under start/stop driving condition, which can cause cathode potential >1.4 V *vs.* reversible hydrogen electrode (RHE) [29]. Carbon materials are commonly used as supports for metal nanoparticles in electrocatalysis for their good conductivity and high surface area [30]. However, due to the weak interaction between carbon and metals, agglomeration and sintering of Pt-based metal nanoparticles occur during fuel cell operation [31]. In addition, carbon corrosion occurs at high potentials, resulting in accelerated loss of Pt surface area and worsened mass transport in the catalyst layer [32–34]. To mitigate these issues, corrosion-resistant materials have been studied for replacing carbon materials as the supports, including metal oxides (e.g., SnO_2, TiO_2, NbO_2) [35–37], carbides (e.g., TiC, WC) [38–40] and nitrides (e.g., TiN, NbN) [41–44]. However, this kind of Pt catalysts usually resulted in low activity which was mainly caused by their low conductivities [45,46]. For example, early studies showed that NbO_2 and NbO are better supports than Nb_2O_5 due to electronic conductivity of Nb oxides decreases with higher oxidation state of Nb, causing lower electrocatalytic

* Corresponding author.
** Corresponding author.
E-mail addresses: jia@bnl.gov (J.X. Wang), zhwchen@uwaterloo.ca (Z. Chen).

https://doi.org/10.1016/j.nanoen.2020.104455
Received 26 November 2019; Received in revised form 2 January 2020; Accepted 3 January 2020
Available online 7 January 2020

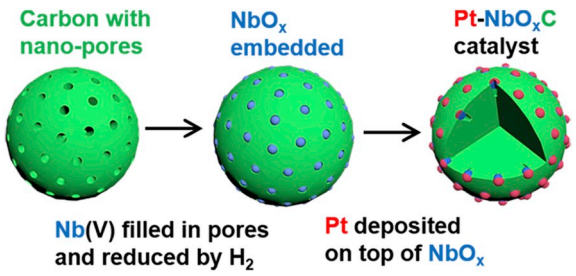

Fig. 1. Schematic illustration of a ~40 nm carbon particle with 4–5 nm surface pores (left), low oxidation-state NbO_x particles embedded into the surface pores on carbon (middle), and Pt-covered NbO_x particles on carbon (right).

activities [36,47]. Furthermore, their ORR activities were getting worse due to their oxidation under high potential and long term running [48,49]. Senevirathne et al. found the formation of electronically insulating surface Nb_2O_5 is the reason for activity fading of Pt/NbO_2 catalyst [45]. Some previous studies used carbon materials and metal-related materials together as supports, however, they did not combine the advantages of these two kinds of supports due to the failure on decreasing metal oxides particle size and the selective Pt distribution on metal oxides, resulting in very little improvement [50,51].

In this study, we demonstrate a new structured Pt/metal oxide/carbon composite catalyst (Pt-NbO_xC), consisting of low-oxidation-state and small NbO_x nanoparticles embedded in nanopores of carbon as nails with fully covered of Pt head shell. As illustrated in Fig. 1, nanopores on carbon surface are utilized to nail-down NbO_x nanoparticles which effectively kept all low-oxidation-state NbO_x particles, formed in hydrogen at 900 °C without overgrowth. Then the fully-covered Pt layers were selectively deposited on top of well dispersed NbO_x particles via spontaneous redox reaction. The obtained catalyst exhibits about 0.56 A mg^{-1} Pt mass activity at 0.9 V vs. RHE, which is about 3 times higher than that of commercial carbon supported Pt catalyst and also excesses the 2020 target of DOE. Furthermore, there are little activity decay and structure change after durability tests for catalysts and supports.

2. Experimental section

2.1. Chemicals

Ketjenblack EC-600JD (KB) was purchased from Akzo Nobel and Vulcan XC-72R (VC) was purchased from Cabot. Niobium (V) chloride ($NbCl_5$, >99.9%), chloroplatinic acid hexahydrate ($H_2PtCl_6{\cdot}6H_2O$, ≥37.50% Pt basis), 2-Propanol ($(CH_3)_2CHOH$, ≥99.5%) and perchloric acid ($HClO_4$, 70%) were purchased from Sigma-Aldrich. Anhydrous ethanol was purchased from Commercial Alcohols. Nafion solution (5% wt) was purchased from Ion Power. All of chemicals were used without further purification.

2.2. Synthesis of NbO_x embedded carbon

Typically, 50 mg dried carbon (Ketjenblack EC-600JD) was immersed in about 2 mL anhydrous ethanol containing 150 μmol $NbCl_5$ in a dried glass vial. The vial was quickly capped to avoid moisture. The volume of solvent to carbon weight ratio was chosen to have the solution completely absorbed into Ketjenblack EC-600JD after 2 h sonication. After drying in vacuum oven at 70 °C for 2 h, the mixture was transferred into a tube furnace. Reduction of Nb precursor was carried out with H_2 at a flow rate of 100 sccm at 220 °C for 1 h, 650 °C for 1 h and 900 °C for 1 h.

2.3. Deposition of Pt on NbO_xC

Pt spontaneous deposition is initiated by low-oxidation-state NbO_x in K_2PtCl_4 aqueous solution without other reducing agent to ensure no Pt nucleation on carbon. Typically, 80 ml ultrapure water in a three-neck flask was heated to 45 °C with N_2 bubbling. Separately, 75 μmol K_2PtCl_4 was dissolved in 20 mL ultrapure water and the solution was also deaerated by N_2 bubbling. A freshly made NbO_xC sample was poured into the three-neck flask while being vigorously stirred, followed by adding the K_2PtCl_4 solution drop by drop. After adding the Pt precursor, the mixture was stirred and kept at 45 °C for about 4 h. Cooled mixture was filtered and rinsed with water. The dried powder was collected as the Pt-NbO_xC catalyst.

2.4. Material characterization

XRD measurements were conducted on a Rigaku MiniFlex X-ray diffractometer, using scanning rate of 1° min^{-1} and with a step of 0.02°. Pt content in catalyst was determined by inductively coupled plasma atomic emission spectroscopy (710-ES, Varian, ICP-OES). X-ray photoelectron spectroscopy (XPS) was performed using Thermo Scientific K-Alpha XPS spectrometer. Pore size analysis was conducted on ASAP 2020 Plus. TEM, HRTEM, HAADF-STEM and EELS- mapping images were performed using JEOL 2100F operated at 200 kV and Hitachi HD2700C STEM equipped with a probe aberration corrector operated at 200 kV. Thermogravimetric analysis (TGA) was conducted on PerkinElmer Thermal Analysis Pyris 1 TGA.

2.5. Electrochemical measurements

Electrochemical experiments were conducted in a three-electrode test cell with 0.1 M $HClO_4$ at 20 °C using a Bio-Logic VSP 300 electrochemistry station. A Pt foil was used as counter electrode and a reversible hydrogen electrode was used as reference electrode. Catalyst ink was prepared with ultrapure water and iso-propanol (v/v = 3:1) and a certain amount of 5 wt% Nafion solution. Working electrodes were prepared by placing 10 μL of catalyst inks on a glassy carbon electrode (d = 5 mm, the geometric electrode area is 0.196 cm^2) and dried in air. The Pt loadings were kept constant at 20 μg cm^{-2} for all samples. Cyclic voltammetry curves were measured from 0.05 V to 1.05 V at a scan rate of 20 mV s^{-1} in N_2-saturated 0.1 M $HClO_4$ solution. Electrochemical surface area (ECSA) was determined by integrated charge for hydrogen desorption between 0.05 and 0.40 V assuming a 210 μC cm^{-2}. The ORR polarization measurements were performed in an O_2-saturated 0.1 M $HClO_4$ solution at 10 mV s^{-1} and with electrode rotation rate at 1600 rpm. The potential cycles used for durability tests were carried out in air-saturated 0.1 M $HClO_4$ solution between 0.6 and 1.0 V at 50 mV s^{-1} and between 1.0 and 1.5 V at 500 mV s^{-1}. For comparison under the same measuring conditions, commercial Pt/C (Tanaka Kikinzoku International Inc., 46.6 wt% Pt, Pt particle size: 2.6 nm) was used as the baseline catalyst.

3. Results and discussion

NbO_x nanoparticles embedded in nanopores of carbon were prepared by sonicating $NbCl_5$ and KB mixture in anhydrous ethanol and annealing in H_2 atmosphere. $NbCl_5$ was firstly changed into $Nb(C_2H_5O)_5$ by reacting with ethanol which is accompanied with the color changing from yellow to colorless. Water in air can lead to formation of the most stable Nb_2O_5 (white solid), and thus, exposure to air needs to be minimized. In a typical synthesis, we sonicated a slurry containing 50 mg carbon (KB) and 150 μmol of Nb(V) precursor in ethanol for about 2 h until liquid was completely absorbed in carbon. After drying the mixture in vacuum oven at 70 °C for 2 h, the sample weight was found significantly lower than that expected for $Nb(C_2H_5O)_5$, but close to that of $Nb(OH)_5$ (Table S1). A possible reaction at temperature below 70 °C is Nb

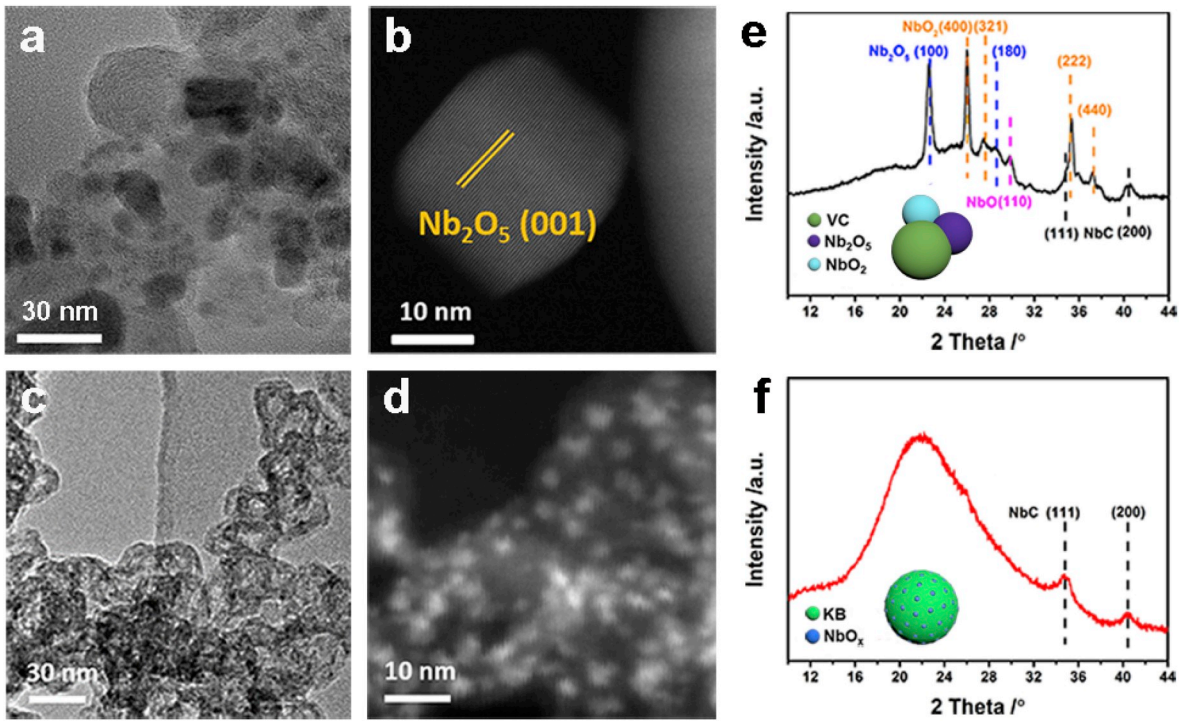

Fig. 2. (a, c) Transmission electron microscopy (TEM) and (b, d) high angle annular dark field scanning TEM (HAADF-STEM) images of samples made by reducing Nb(V) precursors with (a, b) VC and (c, d) KB, Nb has higher electron density than C and appears darker in (a, c) TEM images and brighter in HAADF-STEM images (carbon is essentially invisible), and (e, f) X-ray diffraction profiles for samples made by reducing Nb(V) precursors with (e) VC and (f) KB. Structural models show formation of (e) > 20 nm Nb_2O_5 and NbO_2 particles on VC and (f) < 5 nm NbC (small amount) and amorphous NbO_x (large amount without XRD feature) particles embedded in KB.

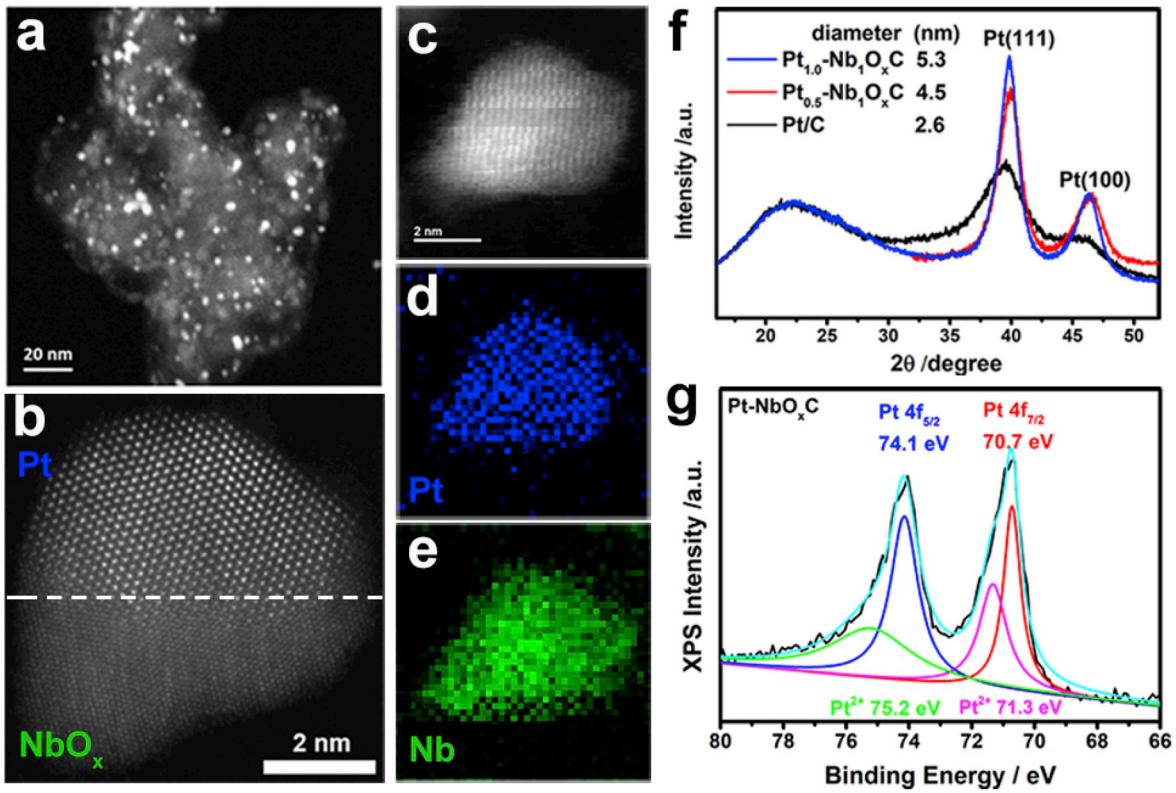

Fig. 3. (a) HAADF-STEM image of as-synthesized Pt-NbO_xC catalyst, (b) HAADF-STEM image of single Pt-NbO_xC nanoparticle in side-view (crystalline Pt head above the dash line and amorphous NbO_x below the dashed line), (c) HAADF-STEM image and (d, e) 2D EELS-mapping of (d) Pt and (e) Nb of a Pt-NbO_x nanoparticle in top-view, (f) XRD profiles of two Pt-NbO_xC samples having Pt:Nb molar ratio 1 and 0.5 in comparison with commercial Pt/C, and (g) Pt 4f XPS spectrum of Pt-NbO_xC.

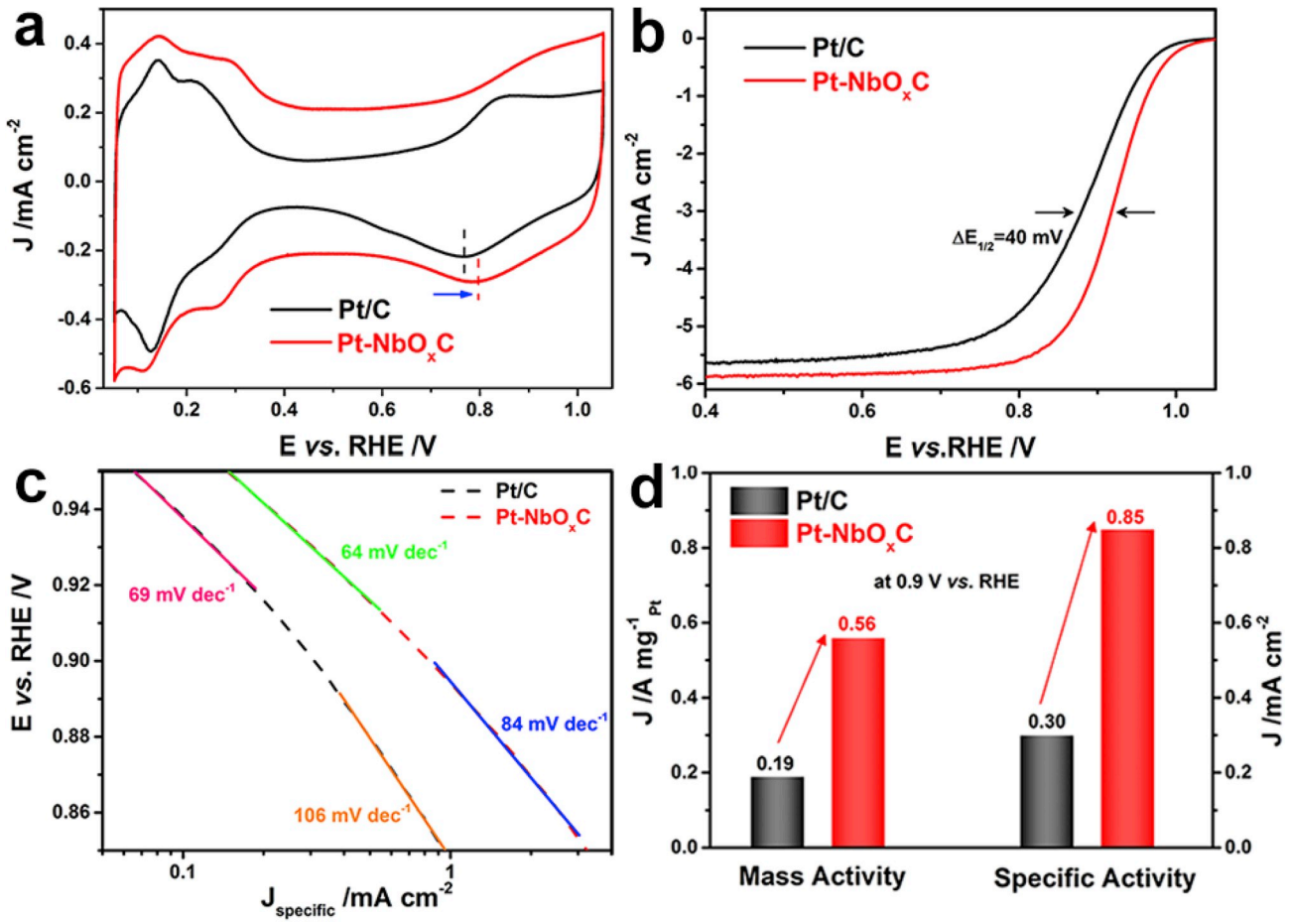

Fig. 4. (a) Cyclic voltammetry curves, (b) ORR polarization curves, (c) Mass transport corrected Tafel plots based on specific current density obtained from ORR polarization curves, and (d) Specific and mass activities at 0.9 V *vs.* RHE of Pt-NbO_xC and commercial Pt/C catalysts for ORR. CV curves were recorded in N_2-saturated 0.1 M $HClO_4$ solution at a sweep rate of 20 mV s^{-1} and ORR polarization curves were recorded at room temperature in an O_2-saturated 0.1 M $HClO_4$ aqueous solution at a sweep rate of 10 mV s^{-1} with rotation rate of 1,600 rpm.

$(C_2H_5O)_5$ + $5C_2H_5OH$ + C = $Nb(OH)_5$–C (solid) + 5C2H5–O–C_2H_5 (diethyl ether, boiling point of 34 °C), but we has not ruled out other gaseous by-products. Running a thermal gravimetric analysis (TGA) for a dried mixture of Nb(V) precursor on carbon found 10.1% weight loss, consistent for 9.8% weight loss expected from a reaction of $2Nb(OH)_5 = Nb_2O_5 + 5H_2O$ (gas), which supports $Nb(OH)_5$ being the precursor before thermal reduction in tube furnace with hydrogen gas flow (Fig. S1). The temperature was raised to 220 °C, 650 °C, and 900 °C with 1 h holding time at each. The gradual rising temperature promotes uniform formation of low-oxidation-state NbO_x.

We found the surface pores of carbon play important roles in forming well dispersed, low oxidation-state NbO_x. Ketjenblack EC-600JD is chosen as the carbon support because it differs from Vulcan XC-72R (very few surface pores) in having many 4–5 nm surface pores. This is evidenced by measured pore size distribution for these two types of carbon powders (Fig. S2). These nano-pores are utilized for controlling the dispersion of Nb precursor, and thus, the particle size of NbO_x. The distinctly different transmission electron microscopy (TEM) images and X-ray diffraction (XRD) profiles of the samples made with VC and KB using the same procedure were showed as Fig. 2. Firstly, Fig. 2a shows that >10 nm Nb oxide particles form on VC, and the lattice spacing of 0.393 nm shown in Fig. 2b corresponds to the spacing between the (001) planes of Nb_2O_5. Sharp XRD diffraction peaks at the primary diffractions for Nb_2O_5 and NbO_2 were observed for the sample made with VC (Fig. 2e). The average particle sizes calculated from the XRD peak widths are >20 nm. In contrast, the NbO_x particles are ≤5 nm in size and densely distributed on carbon surface, consistent with being embedded into the about 4–5 nm pores on the carbon surface (Fig. 2c and d). The lack of strong XRD peaks in Fig. 2f for the sample made with KB suggests that many small and embedded particles are amorphous. The two small diffraction peaks suggest strong interaction between Nb and carbon consistent with NbO_x being embedded in carbon. Deduced from the XRD peak widths and TEM images, > 20 nm Nb_2O_5 and NbO_2 particles on VC are illustrated by the structural model in Fig. 2e. In comparison, TEM images and XRD profile for the sample made with KB support the structural model of embedded ≤5 nm NbO_x on KB as shown in Fig. 2f. Furthermore, we show that confining small amount of Nb precursor in nano-pores on carbon surface not only results in well dispersed small particles, but also facilitates reduction of Nb(V) to low oxidation state. To observe electro-oxidation of low-oxidation-state Nb, we made inks of freshly prepared NbO_x-C samples using ethanol and iso-propanol and measured voltammetry curves in N_2-saturated 0.1 M $HClO_4$. An irreversible Nb oxidation current peak in the first positive potential sweep was observed at 0.8 V (Fig. S3). Previous work with NbO and NbO_2 in the form of thin films reported the peak oxidation potentials at 0.98 V and 1.1 V, respectively [47]. The much lower peak potential in our experiment indicates the lower oxidation state of NbO_x (the oxidation state less 2^+) obtained in H_2 atmosphere at high temperature [36] and NbO_x may be present in oxygen vacancy-rich form of $NbO_{1-\delta}$.

We have found that niobium oxides, such as NbO_2, in which Nb has valence state less than its highest value of 5, have the power to reduce Pt^{2+} or Pt^{4+} into metallic Pt and thus Pt was selectively deposited on the top of oxides (Fig. S4). Therefore, for Pt deposition, we immediately transferred NbO_xC samples after cooling from tube furnace into a

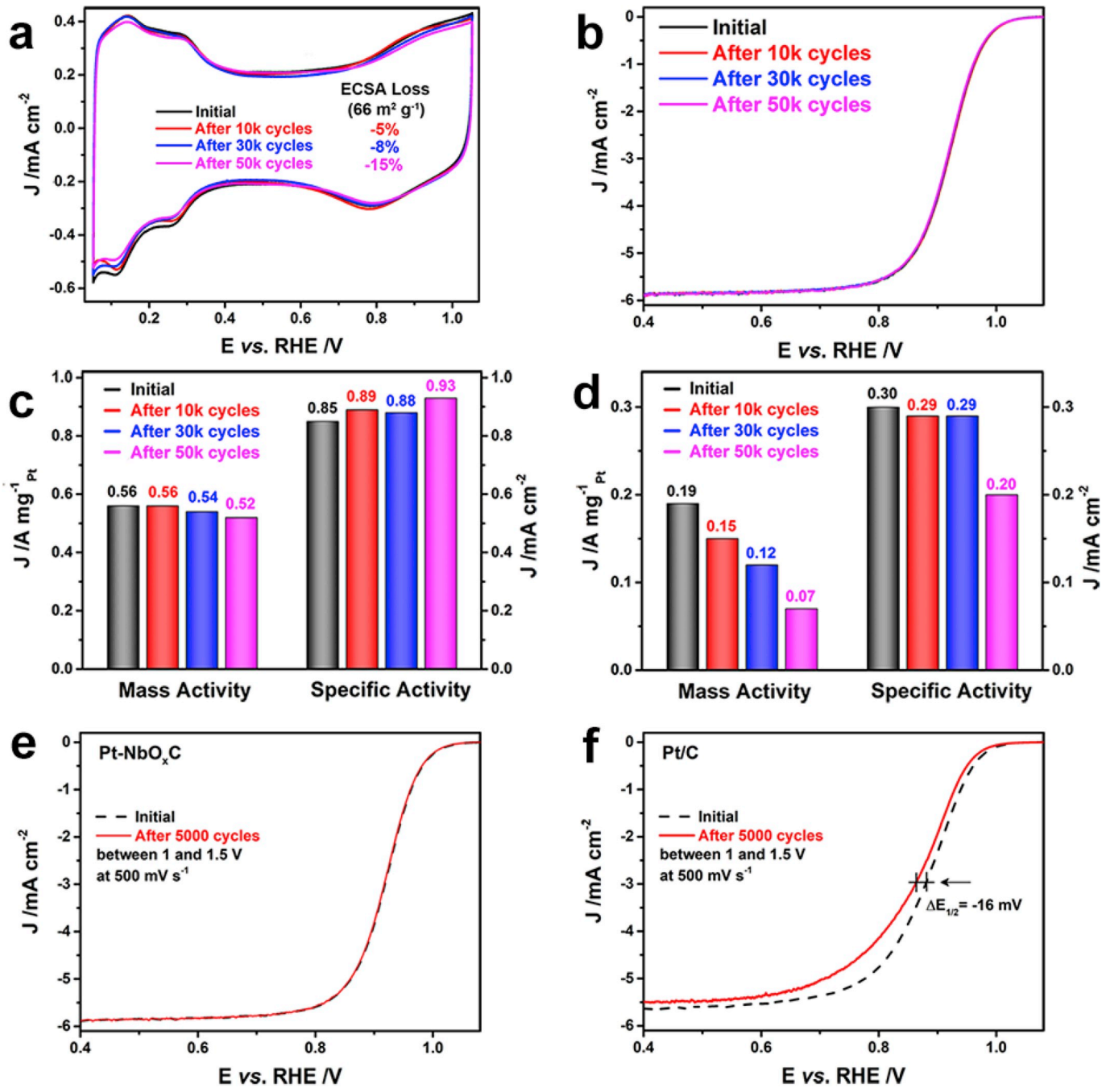

Fig. 5. (a) Cyclic voltammetry curves, (b) ORR polarization curves of Pt-NbO_xC catalyst before and after different number of potential cycles between 0.6 and 1.0 V *vs.* RHE at a sweep rate of 50 mV s^{-1}, Mass and specific activities changes before and after different potential cycles between 0.6 and 1.0 V *vs.* RHE at a sweep rate of 50 mV s^{-1} for (c) Pt-NbO_xC and (d) commercial Pt/C, and ORR polarization curves before and after 5,000 potential cycles between 1 and 1.5 V *vs.* RHE at a sweep rate of 500 mV s^{-1} for (e) Pt-NbO_xC and (f) commercial Pt/C.

deaerated K_2PtCl_4 aqueous solution. In the absence of reducing agent, Pt spontaneous deposition was initiated by partial oxidation of NbO_x and further growth was catalyzed by deposited Pt. As shown by the high angle annular dark field scanning TEM (HAADF-STEM) image in Fig. 3a, the Pt-NbO_x particles remain small and well dispersed. Fig. 3b shows HAADF-STEM image of a single Pt-NbO_x nanoparticle from side view. Pt deposited on embedded NbO_x can be seen by atomically ordered Pt over largely amorphous NbO_x. Fig. 3c–e shows a HAADF-STEM image of a single Pt-NbO_x particle from top view and corresponding electron energy loss spectroscopic (EELS) mapping for Pt and Nb. These images match well in shape and size, indicating formation of complete and uniform thin Pt shell on exposed NbO_x. Thus, the Pt-NbO_xC catalyst is expected to have higher and more sustainable Pt surface area per mass than that expected for 5 nm Pt particles weakly attached on carbon. For two Pt-NbO_xC samples made with Pt:Nb molar ratios being 1 and 0.5 (this ratio is corresponding to the amounts of precursors used in synthesis), all XRD peaks are associated to the face-centered-cubic lattice structure of Pt, consistent with NbO_x being amorphous (Fig. 3f). The lattice constants deduced from the Pt(111) diffraction peak position have 0% and −0.2% strain with respect to the Pt lattice constant of 0.3924 nm. The average Pt particle sizes calculated from the (111) diffraction peak width using Scherer equation are 5.3 and 4.5 nm for Pt:Nb molar ratio 1 and 0.5, respectively. Since the later sample exhibited higher Pt mass activity for ORR, all the data and discussion below are for

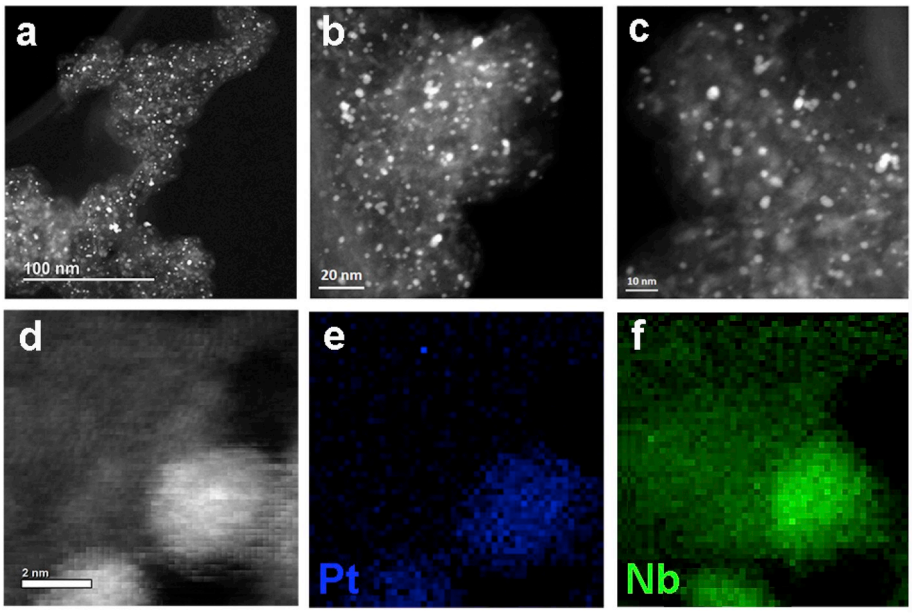

Fig. 6. (a–c) ADF-STEM images Pt-NbO_xC catalyst, and (d) HAADF-STEM image of a Pt-NbO_x nanoparticles, and the corresponding 2D EELS-mapping of (e) Pt, and (f) Nb after 50,000 cycles in the potential between 0.6 and 1.0 V *vs.* RHE with a sweep rate of 50 mV s^{-1}.

Pt:Nb molar ratio of 0.5. The Pt weight percent for the Pt-NbO_xC catalyst is 14.1 wt% Pt, determined by inductively coupled plasma-optical emission spectroscopy (ICP-OES).

Fig. 3g shows X-ray photoelectron spectroscopy (XPS) in the Pt 4f energy region for Pt-NbO_xC. The asymmetry of the Pt 4f doublet is commonly attributed to Pt surface oxidation that results in the shoulder peaks at higher binding energies [52]. Therefore, the lack of significant shoulder on the high BE side for Pt-NbO_xC catalyst compared to commercial Pt/C indicated the increase of metallic Pt surface area. For the deconvoluted Pt $4f_{7/2}$ peak (red line), the binding energy is 70.7 eV that is 0.6 eV lower than the value of 71.3 eV measured for Pt/C (Fig. S6). Previous studies of oxide-supported Pt particles reported a 0.3 eV downshift of the Pt $4f_{7/2}$ peak for Pt on WO_3 and TiO_2, which was attributed to the increased electron density on Pt due to partial charge transfer from oxide supports, indicating the existence of strong metal/support interaction (SMSI) [52]. Recent studies for Pt catalysts with NbO_x on carbon showed no less than 71 eV for Pt $4f_{7/2}$ peak [53,54], and thus, we ascribe the exceptional low value (70.7 eV) for Pt-NbO_xC to the large interface area between thin Pt shells and NbO_x cores made by highly selective Pt deposition on NbO_x. The Nb 3d XPS result indicates the main state of Nb is Nb^{4+} in Pt-NbO_xC after Pt deposition (Fig. S7).

The activity and durability for ORR on the Pt-NbO_xC catalyst was evaluated in 0.1 M $HClO_4$ solution using commercial Pt/C as reference. Firstly, cyclic voltammograms (CVs) were recorded in N_2-saturated 0.1 M $HClO_4$ solution with a scan rate of 20 mV s^{-1} as shown in Fig. 4a. The positive shift of oxide reduction peak potential for Pt-NbO_xC catalyst compared to commercial Pt/C in cathodic scan reveals higher ORR reaction rate due to the decrease of the desorption free energy of Pt–OH, Pt–O, or Pt–O_2 species [55,56]. Besides, Pt-NbO_xC has the ECSA of 66 m^2 g^{-1}_{Pt}, slightly higher than that of Pt/C (63 m^2 g^{-1}_{Pt}). The ORR polarization curve of Pt-NbO_xC catalyst was obtained in an O_2-saturated 0.1 M $HClO_4$ solution at 1,600 rpm with a scan rate of 10 mV s^{-1} after correcting for mass transport limitation. As shown in Fig. 4b, the half wave potential ($E_{1/2}$) of Pt-NbO_xC catalyst is about 918 mV which is 40 mV higher than that of commercial Pt/C catalyst under the same condition. Fig. 4c shows the Tafel slope of Pt-NbO_xC catalyst at the high potential region from 0.95 to 0.85 V with the comparison of commercial Pt/C catalyst. The comparable Tafel slopes of −64 mV dec^{-1} and −84 mV dec^{-1} fitted for Pt-NbO_xC catalyst which are in close agreement with that of commercial Pt/C catalyst, indicating a similar ORR pathway with pure Pt surface. Furthermore, the lower Tafel slopes than that of Pt/C catalyst also indicates an enhancement of the sluggish ORR kinetics [57]. The mass activity of Pt-NbO_xC catalyst is 0.56 A mg^{-1}_{Pt} at 0.9 V *vs.* RHE, which is higher than that of the 2020 U.S. Department of Energy target (0.44 A mg^{-1}_{Pt}) and about 3 times greater than that of commercial Pt/C catalyst (0.19 A mg^{-1}_{Pt}) (Fig. 4d), which nearly the highest activity values among metal oxide containing supported catalysts previously reported (Fig. S8 and Table S2). Its specific activity can reach 0.85 mA cm^{-2} at 0.9 V *vs.* RHE, which is also 3 times higher than that of commercial Pt/C (0.3 mA cm^{-2}). The highly dispersed Pt layer having SMSI effect with NbO_x which maximize Pt utilization and its intrinsic catalysis ability and thus enhances ORR activity [11,58]. The small size and lower-oxidation-state of NbO_x nanoparticles, and close contact with carbon which improve the electric conductivity of whole support also attribute to good ORR activity [36].

The stability of Pt-NbO_xC catalyst was firstly checked by the potential cycling between 0.6 and 1.0 V for up to 50,000 cycles in air-saturated 0.1 M $HClO_4$ solution with a scan rate of 50 mV s^{-1}. Fig. 5a and b shows the CV curves and ORR polarization curves of Pt-NbO_xC catalyst before and after 10,000, 30,000 and 50,000 potential cycles. The loss of ECSA is only −8% and −15% after 30,000 and 50,000 potential cycles compared to a much bigger ECSA loss (44%) for Pt/C after 50,000 cycles (Fig. S9a) while there are no obvious half wave potential decay after 50000 cycles compared to a negative shift in half wave potential (−53 mV) for commercial Pt/C catalyst (Fig. S9b). Furthermore, no current peak due to Nb redox reaction emerging in the 0.4–0.6 V potential region indicated that low-oxidation-state NbO_x did not be oxidized to non-conductive Nb_2O_5 [47].

Fig. 5c shows the mass and specific activities of the Pt-NbO_xC catalyst before and after 10,000, 30,000, and 50,000 potential cycles. After 50,000 cycles, there was only 7.2% loss in mass activity for the Pt-NbO_xC catalyst, while the commercial Pt/C showed a 63% loss of mass activity under the same condition (Fig. 5d) demonstrating excellent durability of the Pt-NbO_xC catalyst. Besides, we also tested the durability of Pt-NbO_xC catalyst under the start/stop driving conditions by running 5,000 potential cycles between 1 and 1.5 V at 500 mV s^{-1}. There is no obvious decay for Pt-NbO_xC catalyst (Fig. 5e), while 16 mV negative shift of half wave potential occurred for commercial Pt/C catalyst (Fig. 5f). We ascribe the excellent durability to the strong Pt binding on embedded NbO_x nanoparticle in carbon, which effectively minimizes

ECSA loss at high potentials in acid by preventing Pt dissolution, particle agglomeration, and carbon corrosion by isolating the contact between Pt and carbon [59,60]. The structural stability of Pt-NbO_xC catalyst after 50,000 of potential cycles was reexamined via microscopic imaging. Fig. 6a–c shows typical HAADF-STEM images of various magnifications (100–10 nm scale bars). There are no significant increase in particle size and decrease in particle density over large area examined, which verifies the absence of particle agglomeration and sintering, Furthermore, 2D-EELS elementals mapping images indicated that the structure of Pt layers oriented on the top of NbO_x are still observed (Fig. 6 d-f).

4. Conclusions

In summary, this study found and verified by various characterization techniques that 4–5 nm surface pores on carbon support (Ketjenblack EC-600JD) can be utilized for nailing down small NbO_x nanoparticles with low-oxidation-state and a fully covered Pt layer on the top of NbO_x nanoparticle can be selectively deposited by NbO_x-initiated Pt^{2+} reduction. The obtained new structured Pt-NbO_xC catalyst shows the mass activities being more than three and seven times of the values for Pt/C catalyst before and after extensive durability tests, respectively. Our study demonstrates ORR activity and durability can be enhanced concurrently by optimizing the structure among Pt, metal oxide and carbon. Furthermore, the method to utilize surface nanopores for highly dispersed metal oxides avoiding overgrowth will be interesting in various applications.

Declaration of competing interest

The authors declare that they have no known competing financial interests or personal relationships that could have appeared to influence the work reported in this paper.

Acknowledgments

Z. M., G.P. J. and Z.W. C. gratefully acknowledge the support provided by the Natural Sciences and Engineering Research Council of Canada, University of Waterloo, and Waterloo Institute for Nanotechnology. The work carried out at Brookhaven National Laboratory in Chemistry, the Center for Functional Nanomaterials, and Condensed Matter Physics and Materials Science is supported by the U.S. Department of Energy under Contract No.DE-SC0012704.

Appendix A. Supplementary data

Supplementary data to this article can be found online at https://doi.org/10.1016/j.nanoen.2020.104455.

References

[1] A. Kulkarni, S. Siahrostami, A. Patel, J.K. Nørskov, Chem. Rev. 118 (2018) 2302–2312.
[2] S. Chu, Y. Cui, N. Liu, Nat. Mater. 16 (2017) 16–22.
[3] Z. Ma, X. Yuan, L. Li, Z.-F. Ma, D.P. Wilkinson, L. Zhang, J. Zhang, Energy Environ. Sci. 8 (2015) 2144–2198.
[4] M. Shao, Q. Chang, J.-P. Dodelet, R. Chenitz, Chem. Rev. 116 (2016) 3594–3657.
[5] V.R. Stamenkovic, D. Strmcnik, P.P. Lopes, N.M. Markovic, Nat. Mater. 16 (2017) 57–69.
[6] B.C.H. Steele, A. Heinzel, Nature 414 (2001) 345–352.
[7] M. Li, Z. Zhao, T. Cheng, A. Fortunelli, C.-Y. Chen, R. Yu, Q. Zhang, L. Gu, B. V. Merinov, Z. Lin, E. Zhu, T. Yu, Q. Jia, J. Guo, L. Zhang, W.A. Goddard, Y. Huang, X. Duan, Science 354 (2016) 1414–1419.
[8] L. Li, S. Shen, G. Wei, X. Li, K. Yang, Q. Feng, J. Zhang, ACS Appl. Mater. Interfaces 11 (2019) 14126–14135.
[9] M.K. Debe, Nature 486 (2012) 43–51.
[10] J.X. Wang, H. Inada, L. Wu, Y. Zhu, Y. Choi, P. Liu, W.P. Zhou, R.R. Adzic, J. Am. Chem. Soc. 131 (2009) 17298–17302.
[11] Z.W. Seh, J. Kibsgaard, C.F. Dickens, I. Chorkendorff, J.K. Nørskov, T.F. Jaramillo, Science 355 (2017), eaad4998.
[12] F. Calle-Vallejo, J. Tymoczko, V. Colic, Q.H. Vu, M.D. Pohl, K. Morgenstern, D. Loffreda, P. Sautet, W. Schuhmann, A.S. Bandarenka, Science 350 (2015) 185–189.
[13] Y.-J. Wang, N. Zhao, B. Fang, H. Li, X.T. Bi, H. Wang, Chem. Rev. 115 (2015) 3433–3467.
[14] L. Zhang, Y. Zhao, M.N. Banis, K. Adair, Z. Song, L. Yang, M. Markiewicz, J. Li, S. Wang, R. Li, S. Ye, X. Sun, Nano Energy 60 (2019) 111–118.
[15] J. Greeley, I.E.L. Stephens, A.S. Bondarenko, T.P. Johansson, H.A. Hansen, T. F. Jaramillo, J. Rossmeisl, I. Chorkendorff, J.K. Nørskov, Nat. Chem. 1 (2009) 552–556.
[16] J. Ying, J. Li, G. Jiang, Z.P. Cano, Z. Ma, C. Zhong, D. Su, Z. Chen, Appl. Catal. B Environ. 225 (2018) 496–503.
[17] M. Lokanathan, I.M. Patil, M. Navaneethan, V. Parey, R. Thapa, B. Kakade, Nano Energy 43 (2018) 219–227.
[18] M. Escudero-Escribano, P. Malacrida, M.H. Hansen, U.G. Vej-Hansen, A. Velázquez-Palenzuela, V. Tripkovic, J. Schiøtz, J. Rossmeisl, I.E.L. Stephens, I. Chorkendorff, Science 352 (2016) 73–76.
[19] S.R. Brankovic, J.X. Wang, R.R. Adžić, Surf. Sci. 474 (2001) L173–L179.
[20] R.R. Adzic, J. Zhang, K. Sasaki, M.B. Vukmirovic, M. Shao, J.X. Wang, A.U. Nilekar, M. Mavrikakis, J.A. Valerio, F. Uribe, Top. Catal. 46 (2007) 249–262.
[21] L. Bu, Q. Shao, B. E, J. Guo, J. Yao, X. Huang, J. Am. Chem. Soc. 139 (2017) 9576–9582.
[22] X. Wang, M. Vara, M. Luo, H. Huang, A. Ruditskiy, J. Park, S. Bao, J. Liu, J. Howe, M. Chi, Z. Xie, Y. Xia, J. Am. Chem. Soc. 137 (2015) 15036–15042.
[23] D. Wang, H.L. Xin, R. Hovden, H. Wang, Y. Yu, D.A. Muller, F.J. DiSalvo, H. D. Abruña, Nat. Mater. 12 (2013) 81–87.
[24] C. Liu, Z. Ma, M. Cui, Z. Zhang, X. Zhang, D. Su, C.B. Murray, J.X. Wang, S. Zhang, Nano Lett. 18 (2018) 7870–7875.
[25] P. Strasser, S. Kühl, Nano Energy 29 (2016) 166–177.
[26] C. Chen, Y. Kang, Z. Huo, Z. Zhu, W. Huang, H.L. Xin, J.D. Snyder, D. Li, J. A. Herron, M. Mavrikakis, M. Chi, K.L. More, Y. Li, N.M. Markovic, G.A. Somorjai, P. Yang, V.R. Stamenkovic, Science 343 (2014) 1339–1343.
[27] W. Gong, Z. Jiang, R. Wu, Y. Liu, L. Huang, N. Hu, P. Tsiakaras, P.K. Shen, Appl. Catal. B Environ. 246 (2019) 277–283.
[28] F. Kong, S. Liu, J. Li, L. Du, M.N. Banis, L. Zhang, G. Chen, K. Doyle-Davis, J. Liang, S. Wang, F. Zhao, R. Li, C. Du, G. Yin, Z. Zhao, X. Sun, Nano Energy 64 (2019) 103890.
[29] C.D. Young, Y.J. Mun, S. Yung-Eun, Adv. Mater. 30 (2018) 1704123.
[30] J.X. Wang, C. Ma, Y. Choi, D. Su, Y. Zhu, P. Liu, R. Si, M.B. Vukmirovic, Y. Zhang, R.R. Adzic, J. Am. Chem. Soc. 133 (2011) 13551–13557.
[31] L.A. Estudillo-Wong, Y. Luo, J.A. Díaz-Real, N. Alonso-Vante, Appl. Catal. B Environ. 187 (2016) 291–300.
[32] X. Yu, S. Ye, J. Power Sources 172 (2007) 145–154.
[33] X. Yu, S. Ye, J. Power Sources 172 (2007) 133–144.
[34] S. Maass, F. Finsterwalder, G. Frank, R. Hartmann, C. Merten, J. Power Sources 176 (2008) 444–451.
[35] F. Takasaki, S. Matsuie, Y. Takabatake, Z. Noda, A. Hayashi, Y. Shiratori, K. Ito, K. Sasaki, J. Electrochem. Soc. 158 (2011) B1270–B1275.
[36] K. Sasaki, L. Zhang, R.R. Adzic, Phys. Chem. Chem. Phys. 10 (2008) 159–167.
[37] A. Bauer, K. Lee, C. Song, Y. Xie, J. Zhang, R. Hui, J. Power Sources 195 (2010) 3105–3110.
[38] I.J. Hsu, D.A. Hansgen, B.E. McCandless, B.G. Willis, J.G. Chen, J. Phys. Chem. C 115 (2011) 3709–3715.
[39] H.-J. Liu, F. Wang, Y. Zhao, H. Fong, Nanoscale 5 (2013) 3643–3647.
[40] Y. Liu, W.E. Mustain, ACS Catal. 1 (2011) 212–220.
[41] B. Avasarala, T. Murray, W. Li, P. Haldar, J. Mater. Chem. 19 (2009) 1803–1805.
[42] Z. Cui, R.G. Burns, F.J. DiSalvo, Chem. Mater. 25 (2013) 3782–3784.
[43] X. Tian, J. Luo, H. Nan, H. Zou, R. Chen, T. Shu, X. Li, Y. Li, H. Song, S. Liao, R. R. Adzic, J. Am. Chem. Soc. 138 (2016) 1575–1583.
[44] Q. Liu, L. Du, G. Fu, Z. Cui, Y. Li, D. Dang, X. Gao, Q. Zheng, J.B. Goodenough, Adv. Energy Mater. 9 (2019) 1803040.
[45] K. Senevirathne, R. Hui, S. Campbell, S. Ye, J. Zhang, Electrochim. Acta 59 (2012) 538–547.
[46] A. Bonakdarpour, R.T. Tucker, M.D. Fleischauer, N.A. Beckers, M.J. Brett, D. P. Wilkinson, Electrochim. Acta 85 (2012) 492–500.
[47] L. Zhang, L. Wang, C.M.B. Holt, T. Navessin, K. Malek, M.H. Eikerling, D. Mitlin, J. Phys. Chem. C 114 (2010) 16463–16474.
[48] D.C. Higgins, J.-Y. Choi, J. Wu, A. Lopez, Z. Chen, J. Mater. Chem. 22 (2012) 3727–3732.
[49] F. Karimi, B.A. Peppley, Electrochim. Acta 246 (2017) 654–670.
[50] W. Sun, J. Sun, L. Du, C. Du, Y. Gao, G. Yin, Electrochim. Acta 195 (2016) 166–174.
[51] M.C. Orilall, F. Matsumoto, Q. Zhou, H. Sai, H.D. Abruña, F.J. DiSalvo, U. Wiesner, J. Am. Chem. Soc. 131 (2009) 9389–9395.
[52] A. Lewera, L. Timperman, A. Roguska, N. Alonso-Vante, J. Phys. Chem. C 115 (2011) 20153–20159.
[53] Q. Jia, S. Ghoshal, J. Li, W. Liang, G. Meng, H. Che, S. Zhang, Z.-F. Ma, S. Mukerjee, J. Am. Chem. Soc. 139 (2017) 7893–7903.
[54] S. Ghoshal, Q. Jia, M.K. Bates, J. Li, C. Xu, K. Gath, J. Yang, J. Waldecker, H. Che, W. Liang, G. Meng, Z.-F. Ma, S. Mukerjee, ACS Catal. 7 (2017) 4936–4946.
[55] J. Hu, L. Wu, K.A. Kuttiyiel, K.R. Goodman, C. Zhang, Y. Zhu, M.B. Vukmirovic, M. G. White, K. Sasaki, R.R. Adzic, J. Am. Chem. Soc. 138 (2016) 9294–9300.
[56] X. Zhao, S. Chen, Z. Fang, J. Ding, W. Sang, Y. Wang, J. Zhao, Z. Peng, J. Zeng, J. Am. Chem. Soc. 137 (2015) 2804–2807.
[57] J.X. Wang, J. Zhang, R.R. Adzic, J. Phys. Chem. A 111 (2007) 12702–12710.

[58] V.T.T. Ho, C.-J. Pan, J. Rick, W.-N. Su, B.-J. Hwang, J. Am. Chem. Soc. 133 (2011) 11716–11724.
[59] Y. Zhang, S. Chen, Y. Wang, W. Ding, R. Wu, L. Li, X. Qi, Z. Wei, J. Power Sources 273 (2015) 62–69.
[60] J. Wang, M. Xu, J. Zhao, H. Fang, Q. Huang, W. Xiao, T. Li, D. Wang, Appl. Catal. B Environ. 237 (2018) 228–236.

Dr. Zhong Ma received his Ph.D. degree from Shanghai Jiaotong University in 2016. Currently, he has been a postdoctoral research fellow with Prof. Zhongwei Chen in the Department of Chemical Engineering at University of Waterloo, Canada. His current work includes design and synthesis of oxygen reduction reaction electrocatalysts.

Dr. Shuang Li received her Ph.D. in 2018 from Institute of Metal Research, Chinese Academy of Sciences. Then she worked as a postdoctoral research fellow in University of Waterloo. Her research interests are mainly focused on microstructure characterization of energy storage materials by using advanced electron microscopy.

Dr. Lijun Wu, is a scientific staff in Condensed Matter Physics and Materials Science Division, Brookhaven National Laboratory, USA. He got his BSc, and MSc in materials science at Shanghai Jiao Tong University, China; Ph.D. in materials science at Hunan University, China. Currently Dr. Wu's research interests focus on the development and application of quantitative transmission electron microscopy techniques, including high resolution transmission electron microscopy, scanning transmission electron microscopy, quantitative electron diffraction and electron energy loss spectroscopy, to solve materials problems in nanomaterials, thermoelectric materials, superconductors and electrode materials in Li-battery.

Dr. Liang Song received his Ph.D. degree from Stony Brook University in 2019. He is currently a visiting scholar working with Dr. Jia X. Wang in Chemistry Division, Brookhaven National Laboratory. His research focuses on developing low platinum-group metal catalysts for the oxygen reduction and ammonia oxidation reactions.

Dr. Gaopeng Jiang received his Ph.D degree on Chemical Engineering (Nanotechnology) in University of Waterloo at 2017, Canada. His research interest mainly focuses on the design and development of nanostructured materials for energy storage and conversion devices including fuel cells, Zn-air batteries, flow batteries and sensors.

Dr. Zhixiu Liang currently works at Condensed Matter Physics & Materials Science, Brookhaven National Laboratory. He received his Ph.D. in chemistry from Stony Brook University under the supervision of Dr. Radoslav R. Adzic from Brookhaven National Laboratory. His research is focusing on advanced in-situ and operando TEM applications on electrochemical system and MeV-ultrafast electron diffraction.

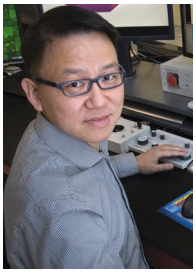

Dr. Dong Su is a Professor at Institute of Physics (IOP), Chinese Academy of Sciences (CAS). He is also an adjunct professor in the Department of Materials Science and Engineering at Stony Brook University since 2011. He got his B.S. in 1998 from Nanjing University. He got his Ph.D in condensed matter physics in 2003, from Nanjing University and IOP, CAS. After doing postdoc in EPFL, Switzerland, University of Illinois at Urbana-Champaign, and Arizona State University, he joined Brookhaven National Laboratory in 2008 as an assistant scientist in Center for Functional Nanomaterials (CFN). He has been through the rank and was promoted to scientist with continuing appointment in 2015 and in 2019, he was the group leader of electron microscopy in CFN. Dr. Dong Su has published more than 300 papers in peer-reviewed journals with citation >19,000.

Dr. Yimei Zhu is Senior Physicist at Brookhaven National Laboratory (BNL) and Adjunct Professor at Columbia University and Stony Brook University. He received his PhD from Nagoya University and joined BNL as Assistant Scientist in 1988, rising through the rank to become Tenured Senior Physicist in 2002. Zhu has published 600 peer-reviewed journal articles and delivered more than 300 invited talks at international conferences. His research interests include condensed matter physics of correlated electron systems and advanced electron microscopy in materials characterization as well as microscopy method and instrumentation. He is an elected Fellow of APS, MSA, AAAS and MRS.

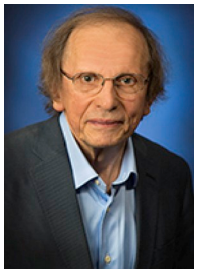

Dr. Radoslav R. Adzic is a Senior Chemist Emeritus at Brookhaven National Laboratory and Adjunct Professor Stony Brook University. He graduated from the University of Belgrade in 1974 with a Ph.D. in chemistry. He was director of Institute of Electrochemistry and professor Univversity of Belgrade. He is a Fellow of the Electrochemical Society and of International Society of Electrochemistry. He is correspondent member of the Serbian Academy of Arts and Sciences, Foreign Member of Academy of Engineering Science of Serbia, Member, International Academy of Electrochemical Energy Science. He has more than 300 scientific publications in the field of surface electrochemistry and electrocatalysis and 20 U S. patents. Some of his awards include, Science and Technology Award from Brookhaven National Laboratory 2005, SciAm 50 Award 2007, the U.S. Department of Energy's Hydrogen R&D Award in 2008 and in 2012, The "R&D 100". Symposium Electrocatalysis 9 at 333rd Electrochemical Society Meeting honoring Radoslav to Adzic. Thomson Reuters a Highly cited researcher, 2016, 2017, 2018.

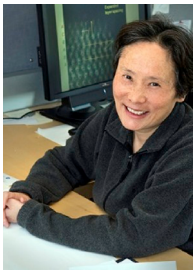

Dr. Jia X. Wang is a staff scientist at Brookhaven National Laboratory. She received her Ph. D. degree in physical chemistry from City University of New York in 1987. After two years at Princeton University as a postdoctoral researcher, she came to Brookhaven National Laboratory in 1989. She firstly studied surface electrochemistry on single crystals using synchrotron X-diffraction techniques and then mainly involved in studying electrocatalysis and developing advanced nanocatalysts for fuel cell and water electrolyzers.

Dr. Zhongwei Chen is Canada Research Chair Professor in Advanced Materials for Clean Energy at University of Waterloo. His research interests are in the development of advanced energy materials for metal-air batteries, lithium-ion batteries and fuel cells. He has published 1 book, 7 book chapters and more than 250 peer reviewed journalarticles with over 20 000 citations with H-index 70 (GoogleScholar). He is also listed as inventor on 20 US/international patents, with several licensed to companies in USA and Canada. He was recipient of the 2016 E. W. R SteacieMemorial Fellowship, which followed shortly upon several other prestigious honors, including the Ontario Early Researcher Award, an NSERC Discovery Supplement Award, the Distinguished Performance and the Research Excellence Awards from the University of Waterloo.